# Coefficients of reaction-diffusion processes derived from patterns in rocks

Chong Liu[1], Victor Calo[2], Klaus Regenauer-Lieb[2], and Manman Hu[3]

[1]The University of Hong Kong
[2]Curtin University
[3]University of Hong Kong

January 20, 2023

**Abstract**

Self-organizing diffusion-reaction systems naturally form complex patterns under far from equilibrium conditions.
A representative example is the rhythmic concentration pattern of Fe-oxides in Zebra rocks; these patterns include reddish-brown stripes, rounded rods, and elliptical spots. Similar patterns are observed in the banded iron formations which are presumed to have formed in the early earth under global glaciation. We propose that such patterns can be used directly (e.g., by computer-vision-analysis) to infer basic quantities relevant to their formation giving information on generalized chemical gradients. Here we present a phase-field model that quantitatively captures the distinct Zebra rock patterns based on the concept of phase separation that describes the process forming Liesegang stripes. We find that diffusive coefficients (i.e., the bulk self-diffusivities and the diffusive mobility of Cahn-Hilliard dynamics) play an essential role in controlling the appearance of regular stripe patterns as well as the transition from stripes to spots. The numerical results are carefully benchmarked with the well-established empirical spacing law, width law, timing law and the Matalon-Packter law. Using this model, we invert for the important process parameters that originate from the intrinsic material properties, the self-diffusivity ratio and the diffusive mobility of Fe-oxides, with a series of Zebra rock samples. This study allows a quantitative prediction of the generalized chemical gradients in mineralized source rocks without intrusive measurements, providing a better intuition for the mineral exploration space.

# Coefficients of reaction-diffusion processes derived from patterns in rocks

**Chong Liu[1,3], Victor M. Calo[2], Klaus Regenauer-Lieb[3,4], Manman Hu[1]**

[1]Department of Civil Engineering, The University of Hong Kong, Hong Kong, China
[2]School of Electrical Engineering, Computing and Mathematical Sciences, Curtin University, P.O. Box U1987, Perth, WA 6845, Australia
[3]WA School of Mines: Minerals, Energy and Chemical Engineering, Curtin, Bentley, WA 6102, Australia
[4]School of Minerals and Energy Resources Engineering, UNSW, Sydney, NSW 2052, Australia

**Key Points:**

- Inversion of Cahn-Hilliard dynamic coefficients from photographic images of striped patterns is shown to be accurate;
- Transition from stripes to spots is triggered by low reaction Cahn-Hilliard product mobility (here hematite);
- Application of computer-vision algorithms in conjunction with inversion may allow novel geophysical exploration tools for ores.

Corresponding author: Manman Hu, mmhu@hku.hk

**Abstract**

Self-organizing diffusion-reaction systems naturally form complex patterns under far from equilibrium conditions. A representative example is the rhythmic concentration pattern of Fe-oxides in Zebra rocks; these patterns include reddish-brown stripes, rounded rods, and elliptical spots. Similar patterns are observed in the banded iron formations which are presumed to have formed in the early earth under global glaciation. We propose that such patterns can be used directly (e.g., by computer-vision-analysis) to infer basic quantities relevant to their formation giving information on generalized chemical gradients. Here we present a phase-field model that quantitatively captures the distinct Zebra rock patterns based on the concept of phase separation that describes the process forming Liesegang stripes. We find that diffusive coefficients (i.e., the bulk self-diffusivities and the diffusive mobility of Cahn-Hilliard dynamics) play an essential role in controlling the appearance of regular stripe patterns as well as the transition from stripes to spots. The numerical results are carefully benchmarked with the well-established empirical spacing law, width law, timing law and the Matalon-Packter law. Using this model, we invert for the important process parameters that originate from the intrinsic material properties, the self-diffusivity ratio and the diffusive mobility of Fe-oxides, with a series of Zebra rock samples. This study allows a quantitative prediction of the generalized chemical gradients in mineralized source rocks without intrusive measurements, providing a better intuition for the mineral exploration space.

## Plain Language Summary

Patterns in nature are observed in disparate fields of science in biology, geology, mechanics, atmospheric physics, chemistry and others. A unifying principle to decipher those patterns is using a reaction-diffusion approach, as employed here, which when implemented in numerical simulations can deliver a perfect match to those observed in nature. Here we go one step further and show that dynamic coefficients describing the concentrations of valuable species such as hematite can be derived from the images. The proposed algorithms is benchmarked here on the Zebra banded rock in Western Australia. The broader impact of the presented work is the development of a future exploration tool, based on computer-vision, revealing high grades of iron in the prominent worldwide banded iron formations which bear similar characteristic stripes. Our models also capture the interesting phenomenon of transition from bands to spots that has not been addressed before.

## 1 Introduction

Self-organization develops autonomously in reaction-diffusion systems and is observed in many disciplines (e.g., pattern formation in biology (Cooper, 2012), corrosion processes and electrochemical deposition in chemistry (Christoph et al., 1999; Nakouzi & Sultan, 2011; Arguello, Labanda, et al., 2022; Arguello, Gumulya, et al., 2022), and Zebra striped formation and rock textures in geology (Wang et al., 2015; Msharrafieh et al., 2016; Kelka et al., 2017; Abrajevitch et al., 2018; May et al., 2019; Al-Ghoul & Sultan, 2019; Regenauer-Lieb et al., 2021)). Two necessary conditions are required to induce self-organization: (i) the governing chemical reactions and diffusion processes are far from the equilibrium; and (ii) at least two processes actively interact in the reaction-diffusion system, which is an open system. Herein, we present a study on the specific self-organizing system producing rhythmic concentration patterns of Fe-oxides (hematite) that commonly seen in sedimentary rocks. The formation of hematite is attributed to the oxidation of the ferrous ions in the groundwater according to the following chemical reaction

$$2\mathrm{Fe}^{2+} + \mathrm{O}^{2-} + 2\mathrm{H_2O} \rightarrow \text{hematite: } \mathrm{Fe_2O_3} + 4\mathrm{H}^{+}$$

A unique hematite pattern observed in Zebra rocks from a relatively small area in the Western Australian East Kimberley region has attracted heated attention (Loughnan & Roberts, 1990). Most Zebra rock patterns appear as reddish brown stripes, rounded rods, and elliptical spots against the background. The red and brown structures have similar mineral compositions, while the latter is rich in ferric oxide concentration. Although the Zebra rock patterns were discovered and described over two centuries ago, an operative mechanism detailing their formation process is still lacking.

Previous pattern formation investigations in Zebra rocks include field, experimental, and theoretical analyses. In early studies, Larcombe (1924, 1926) and Geidans (1981) suggested that the sedimentation processes, either in marine environments or ripple troughs, are responsible for the regular hematite precipitation based on the petrographic examination of Zebra rocks from the field. Hobson (1930) conducted a mineral analysis but found little evidence to support the theory of sedimentation, without providing an alternative explanation. Later, Hancock (1968) proposed to explain the Zebra patterns by a post-depositional leaching theory. In his theory, groundwater circulation transports the iron and re-precipitates it into periodic patterns along the bedding and joint planes. However, this is contrary to the observation, as precipitation patterns also emerge in intact rocks. In 1990, Loughnan and Roberts (1990) linked the Zebra pattern formation to the Liesegang striping theory after reexamining the mineral compositions of intact Zebra rocks. They found that pH fluctuations induced by oxidation decomposition of pyrite would create a favorable chemical environment to convert ferrous to colloidal hematite ($Fe_2O_3$). The concentration growth hence results in Liesegang striping due to the periodic coagulation of an autocatalytic nucleation mechanism. Kawahara et al. (2022) criticized this model as pyrite is found in Zebra rocks suggesting an acidic fluid environment. They thereby proposed a new formation mechanism arguing that the pH fluctuations are due to the neutralization reactions between an $Fe^{2+}$-bearing acidic hydrothermal fluid and the carbonate minerals in the sedimentary rock. Accordingly, the Fe-precipitation was postulated to form the characteristic rhythmic striping patterns in the wake of the iron concentration front. This model is coined as the Liesegang precipitation model.

Shortcomings of the above-described earlier studies include: (1) lacking a quantitative description of the pattern formation; (2) lacking a mathematical model to test predictions, and (3) neglecting the variety of patterns observed in Zebra rocks. In particular, the transition to spotted patterns and the combined patterns with the bands and spots is not addressed. We solve these shortcomings by first casting the Liesegang hypothesis into a concise thermodynamic basis following the classical Cahn-Hilliard description (Cahn & Hilliard, 1958) and a subsequent modeling of Zebra rock pattern formations based on the Liesegang striping theory.

Several celebrated theoretical models have sought to describe the mechanism underlying the Liesegang phenomenon since first described in the late 1800s (Liesegang, 1906). In 1897, Wilhelm Ostwald proposed a supersaturation model where the nucleation and depletion govern the periodic precipitation (Ostwald, 1902; Büki et al., 1995; Antal et al., 1998). An external electrolyte diffuses into the gel and reacts with the inner electrolyte, increasing the product concentration locally. After the product concentration exceeds a threshold supersaturation value, the product eventually nucleates, grows, aggregates, and forms periodic precipitation stripes. Although the supersaturation theory can simulate the qualitative Liesegang features, it cannot explain many experimental findings, such as the gravity-dominated Liesegang bands (Holba & Fusek, 2000). Hedges and Henley suggested a sol coagulation theory to fill this gap (Hedges & Henley, 1928). The sol coagulation model explains the formation of the distinct precipitation as a two-step process: first, the colloidal sol is created but invisible to the naked eye; with the colloidal sol increasing regionally, the visible precipitation stripes emerge when ion strength approaches the critical coagulation concentration (Müller et al., 1982). However, neither the supersaturation theory or the sol coagulation theory can explain the transition from

the stripes to the spots. In 1999, a phase separation theory was proposed to describe the formation of Liesegang patterns (Antal et al., 1999, 2001; Hantz & Biró, 2006; Thomas et al., 2013; Dayeh et al., 2014). In this model, pattern formation appears as a result of the spinodal decomposition of the product, i.e., the diffusion front transforms the system between the spinodal points when the product concentration is initially in a stable or metastable state, leading to pattern forming instabilities.

The phase separation model is widely used for its simple concept and capability of simulating irregular patterns as well as the transition between stripes and spots by introducing noise effects (Thomas et al., 2013; Dayeh et al., 2014). It has also shown its robustness in simulating the Liesegang type patterns in many emerging fields of soft-matter and chemical-biology (Badr et al., 2011; Nakouzi & Steinbock, 2016; Morsali et al., 2020). Here the concept of phase separation is employed for interpretation and parameter inversion of the rhythmically banded and spotted patterns of East Kimberley Zebra rocks, which can be readily extended to the general classification of Mississippi Valley Type deposits (Wang et al., 2015; Kelka et al., 2017).

## 2 Methodology

### 2.1 Governing equations

The classical phase separation concept is used to explain the Liesegang pattern formation in a reaction-diffusion system. Generically, we consider two reagents $A$ and $B$ ($O^{2-}$ and $Fe^{2+}$, respectively, in the current study) that react producing $C$ (i.e., $Fe_2O_3$) in the wake of a moving diffusion front: $A + B \rightarrow C$, defined as a second-order, the solely irreversible reaction in a medium. The corresponding two reaction-diffusion equations read

$$\begin{aligned} \frac{\partial a}{\partial t} &= D_a \ \Delta a - \kappa ab \\ \frac{\partial b}{\partial t} &= D_b \ \Delta b - \kappa ab \end{aligned} \tag{1}$$

where $a$ and $b$ denote the concentration of the reagents A and B, respectively. $\Delta$ is the Laplacian, $\kappa$ the reaction rate, and $D_a$ and $D_b$ the self-diffusion coefficients of the reagents A and B, respectively. The phase separation model assumes that the reaction product $C$ separates into two distinct phases: low- and high-concentration phases, instead of forming intermediate complexes (Antal et al., 1999). The concentration contrast between phases leads to the forming of the precipitation patterns, underpinned by the Cahn-Hilliard equation (Cahn & Hilliard, 1958; Cahn, 1961):

$$\frac{\partial c}{\partial t} = \ \nabla \cdot (\lambda \nabla \mu) + \kappa ab + \eta_c \tag{2}$$

where $c$ denotes the concentration of the product C, $\lambda$ the diffusive mobility of the product. $\kappa ab$ represents the rate of production $C$ particles at the reaction-diffusion front, and $\eta_c$ denotes possible noise effects, including the inhomogeneity introduced by the initial concentration of constituents, thermal fluctuation of the system, influx from the environment, etc. $\mu$ is the total free energy density characterised by a generalised chemical potential (Cahn & Hilliard, 1958) that drives the phase separation, which consists of two components: the bulk free energy density $f_{,c}$ and the interfacial energy density $\sigma \Delta c$ written as

$$\mu = f_{,c} - \sigma \Delta c \tag{3}$$

in which $\sigma$ is the gradient parameter related to the thickness of the interfaces. $f$ and $f_{,c}$ are the bulk free energy and its density, respectively. When reactions can turn the material into "active matter", an effective nonequilibrium chemical potential needs to be formulated to account for the potential microscopic violation of the action-reaction symmetry. We are seeking here the simplest model that can quantitatively describe the patterns formed in Zebra rocks and do not consider this interesting possibility for forma-

tion of dynamic patterns in the form of excitation waves (Hu et al., 2022; Regenauer-Lieb et al., 2021).

The bulk free energy $f$ has two minima in the equilibrium states, associated with the low and high concentrations (denoted as $c_l$ and $c_h$, respectively) of the production $C$. For simplicity, we use a Landau-Ginzburg type free energy $f$ with the minima at $c_l$ and $c_h$ and the maximum $\bar{c} = (c_l + c_h)/2$ as shown in Figure 1.

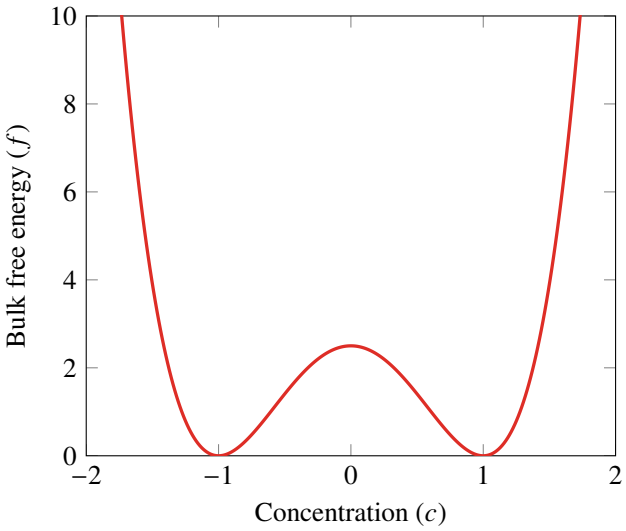


**Figure 1.** Schematic of the double-well bulk free energy profile against concentration, with two minima at $c_l$ and $c_h$ and one maximum at $\bar{c} = (c_l + c_h)/2$.

$$f = -\frac{\varepsilon}{2}(c - \bar{c})^2 + \frac{\gamma}{4}(c - \bar{c})^4 \tag{4}$$

where $\varepsilon$ and $\gamma$ are system-dependent parameters and $\sqrt{\varepsilon/\gamma}$ determines the minima of the bulk free energy $f$. Both $\varepsilon > 0$ and $\gamma > 0$ are required (see Figure 1) to induce phase separation in the system.

The generalized chemical potential hence writes as

$$\mu = -\varepsilon(c - \bar{c}) + \gamma(c - \bar{c})^3 - \sigma\Delta c \tag{5}$$

We rewrite (1) and (2) in a dimensionless form by defining the normalized concentration, time, and length scales as

$$\hat{c} = \frac{c_h - c_l}{2}, \quad \tau = \frac{1}{k\hat{c}}, \quad l = \sqrt{\frac{D}{k\hat{c}}}b \tag{6}$$

and shifting the normalized concentration as

$$m = \frac{c - \bar{c}}{\hat{c}} \approx \frac{c}{\hat{c}} - 1. \tag{7}$$

Eventually we obtain the dimensionless final set of equations governing the pattern-forming process:

$$\begin{aligned}
\frac{\partial a}{\partial t} &= D_a\ \Delta a - \kappa a b \\
\frac{\partial b}{\partial t} &= D_b\ \Delta b - \kappa a b \\
\frac{\partial m}{\partial t} &= \nabla \cdot (\lambda\, \nabla\, \mu) + \kappa a b + \eta_c \\
\mu &= -\varepsilon m + \gamma m^3 - \sigma \Delta m
\end{aligned} \tag{8}$$

where $\sigma = \sigma_0 k\hat{c}/D\varepsilon$ denotes the normalized gradient parameter. Note that $\lambda = \lambda_0\varepsilon/D$ and $\eta_c = \eta_{c0}/k\hat{c}^2$ are now redefined as the normalized diffusive mobility, and normalized noise parameter, of the product, respectively.

### 2.2 Problem statement

Considering a 2D initial–boundary value problem in a rectangular domain, we denote the domain as $\Omega \in \mathbb{R}^2$ and its boundary with a unit outward normal vector $\mathbf{n}$ as $\Gamma$. We impose essential and natural boundary conditions for the A and B reagents, the compound C, and the generalised chemical potential $\mu$ as well as $\Gamma_a$, $\Gamma_b$, $\Gamma_m$, and $\Gamma_\mu$ defining the essential boundaries for the reagents A, B, C and $\Gamma_p$, $\Gamma_q$, $\Gamma_r$, and $\Gamma_t$ as the natural boundaries.

These decomposed essential and natural boundaries satisfy

$$\begin{aligned}
\overline{\Gamma_a \cap \Gamma_p} = \overline{\Gamma_b \cap \Gamma_q} = \overline{\Gamma_m \cap \Gamma_r} = \overline{\Gamma_\mu \cap \Gamma_t} = \emptyset \\
\overline{\Gamma_a \cup \Gamma_p} = \overline{\Gamma_b \cup \Gamma_q} = \overline{\Gamma_m \cup \Gamma_r} = \overline{\Gamma_\mu \cup \Gamma_t} = \Gamma
\end{aligned} \tag{9}$$

The essential boundary conditions contain

$$a = \bar{a}\ \text{ on }\ \Gamma_a;\ \ b = \bar{b}\ \text{ on }\ \Gamma_b;\ \ m = \bar{m}\ \text{ on }\ \Gamma_m;\ \ \mu = \bar{\mu}\ \text{ on }\ \Gamma_\mu. \tag{10}$$

and the natural boundary conditions include

$$\begin{aligned}
\nabla a \cdot \mathbf{n} = j_a\ \text{ on }\ \Gamma_p;\ \ \nabla b \cdot \mathbf{n} = j_b\ \text{ on }\ \Gamma_q; \\
\nabla m \cdot \mathbf{n} = j_m\ \text{ on }\ \Gamma_r;\ \ \nabla \mu \cdot \mathbf{n} = j_\mu\ \text{ on }\ \Gamma_t.
\end{aligned} \tag{11}$$

In addition, the initial conditions are

$$a|_{t=0} = a_0;\ \ b|_{t=0} = b_0;\ \ m|_{t=0} = m_0;\ \ \mu|_{t=0} = \mu_0 \quad \text{in}\ \ \Omega\,. \tag{12}$$

### 2.3 Computational methods

We solve the coupled nonlinear partial differential equations (8) using an open-source high-performance phase-field code, PRISMS-PF (DeWitt et al., 2020) based on the finite element library of `deal.II` (Arndt et al., 2020). The library supports adaptive mesh refinement, massively parallel, and matrix-free finite element simulation. We derive the weak formulation to the coupled equations (8) with the boundary and initial conditions (10)–(12) using the following trial functions

$$\mathcal{S}_i := \{i : \Omega \to \mathbb{R} \mid i \in H^1,\ i = \bar{i}\ \text{ on }\ \Gamma_i\},\ i \in \{a, b, m, \mu\}$$

and test functions

$$\mathcal{V}_i := \{j : \Omega \to \mathbb{R} \mid j \in H^1,\ j = 0\ \text{ on }\ \Gamma_i\},\ j \in \{\phi, \psi, \eta, \omega\}$$

and integration by parts. By adopting the forward Euler method for time discretization, the corresponding weak forms become

$$\int_\Omega \phi a^{n+1}\, dV = \int_\Omega \phi \underbrace{(a^n - \Delta t \kappa a^n b^n)}_{r_a} - \nabla \phi \underbrace{\Delta t D_a \cdot (\nabla a^n)}_{r_{ax}}\, dV \tag{13}$$
$$+ \int_\Gamma \phi(\Delta t D_a) j_a^n\, dS$$
$$\int_\Omega \psi b^{n+1}\, dV = \int_\Omega \psi \underbrace{(b^n - \Delta t \kappa a^n b^n)}_{r_b} - \nabla \psi \underbrace{\Delta t D_b \cdot (\nabla b^n)}_{r_{bx}}\, dV \tag{14}$$
$$+ \int_\Gamma \psi(\Delta t D_b) j_b^n\, dS$$
$$\int_\Omega \omega m^{n+1}\, dV = \int_\Omega \omega \underbrace{(m^n + \Delta t \kappa a^n b^n + \Delta t \eta_c)}_{r_m} - \nabla \omega \underbrace{\Delta t \cdot (\lambda \nabla \mu^n)}_{r_{mx}}\, dV \tag{15}$$
$$\int_\Omega \eta \mu^{n+1}\, dV = \int_\Omega \eta \underbrace{\left(-\varepsilon m^n + \gamma (m^n)^3\right)}_{r_\mu} + \nabla \eta \cdot \underbrace{\sigma \nabla m^n}_{r_{\mu x}}\, dV \tag{16}$$

The numerical analysis presented as follows is based on an implementation of (13)-(16) in PRISMS-PF, which allows for future extensions of this study to a 3D scenario with its adaptive mesh refinement feature.

## 3 Numerical results

We first verify the phase separation model presented in Section 2. A Liesegang band evolution is simulated where the noise effects are absent, as presented in Section 3.1. Our analysis shows that our numerical model reproduces four empirical laws supported by experiments, namely the timing law, the spacing law, the Matalon-Packter law, and the width law. The numerical investigation adopts a pseudo-1D solution strategy (1D solution of a single column of quadrilateral elements) for numerical efficiency in mesh refinement studies. The pseudo-1D models were found to deliver identical results to their true 2D counterparts for the scaling law analysis. Subsequently, in Section 3.2, we perform a parameter study of the effect of diffusive coefficients on the spacing law. The key diffusional coefficients include the ratio of the self-diffusion coefficients $D_a/D_b$ and the Cahn-Hilliard diffusive mobility $\lambda$. Finally, we present the simulation of the diverse patterns observed in Zebra rocks, i.e., regular stripes (including uniform stripes) in Section 3.3 and irregular patterns containing stripes and spots in Section 3.4.

### 3.1 Numerical validation

The first example demonstrates the capacity of the phase separation model in terms of governing the formation of regular Liesegang stripes and yielding four well-established empirical laws calibrated by laboratory experiments. The domain selected for study is a rectangle with the height $L_x$ and the width $L_y$ as shown in Figure 2a. For the validation and parameter studies, we simulate both pseudo-1D (a single row of quadrilateral elements) and real 2D domains and compare their results. The domain size for the pseudo-1D and 2D are $L_x = 320 \times L_y = 0.125$ and $L_x = 320 \times L_y = 32$, respectively. Periodic boundary conditions are applied in the $y$-direction on the vertical boundaries and no-flux boundary conditions $j_a = j_b = j_m = j_\mu = 0$ on the bottom boundary. At the top boundary, we adopt a constant concentration $\bar{a} = 100$ for the reagent $A$ by the Dirichlet boundary condition, with no-flux boundary conditions $j_b = j_m = j_\mu = 0$ for other variables. The initial conditions are $a_0 = 0$, $b_0 = 1.0$, and $m_0 = -1.0$. Regular Liesegang striping patterns are generated by neglecting the noise effect (i.e., $\eta_c$ vanishes). We use

a uniform grid of 2560×1 for the pseudo-1D problem and 2560×256 for the 2D problem with a time step of $\Delta t = 2.5 \times 10^{-5}$. Table 1 lists the parameters used.

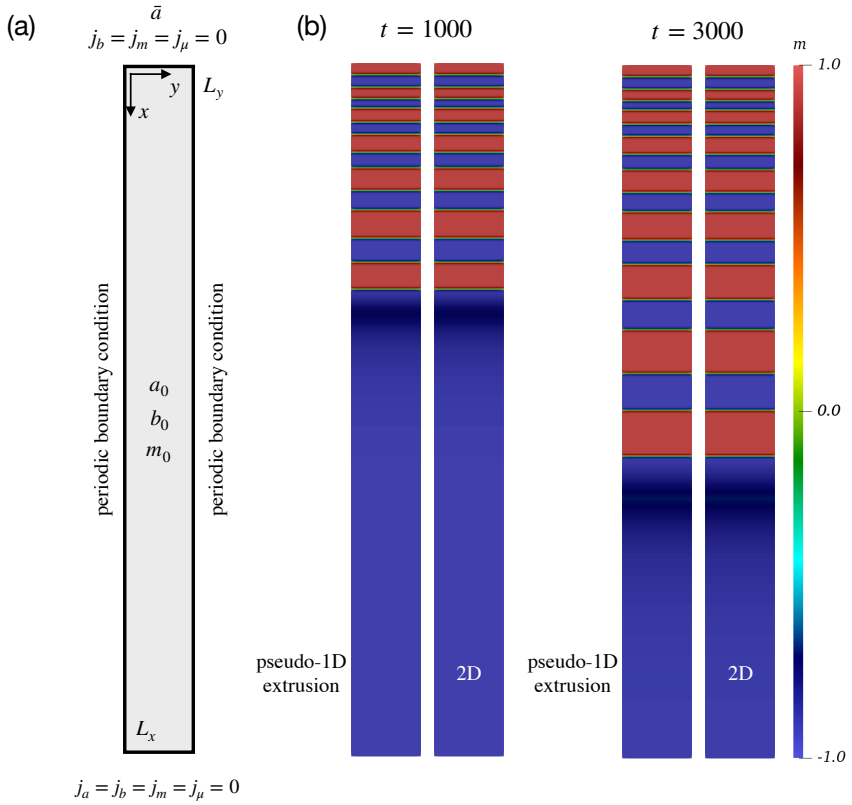


**Figure 2.** Liesegang striping: a) Schematic of the numerical setup and b) comparison of the distribution of $m$ between the pseudo-1D-extrusion and 2D cases at time $t = 1000$ and $t = 3000$. These pseudo-1D results extrude $L_y = 0.125$ to $L_y = 32$ along the $y$-direction.

**Table 1.** Material properties for Liesegang band simulation.

| Properties | Values |
|---|---|
| Diffusion coefficient $D_a$ | 1.0 |
| Diffusion coefficient $D_b$ | 1.0 |
| Reaction rate $\kappa$ | 1.0 |
| Diffusive mobility $\lambda$ | 1.0 |
| Parameter $\varepsilon$ | 1.0 |
| Parameter $\gamma$ | 1.0 |
| Gradient parameter $\sigma$ | 0.2 |
| Noise effect parameter $\eta_c$ | 0 |

Figure 2b displays the distribution of the normalized product concentration $m$ at time $t = 1000$ and $t = 3000$ for the pseudo-1D extrusion to 256 quadrilateral elements as the reference 2D scenario. Periodic precipitation bands with increasing width are generated as the reaction-diffusion front propagates, forming regular Liesegang band pat-

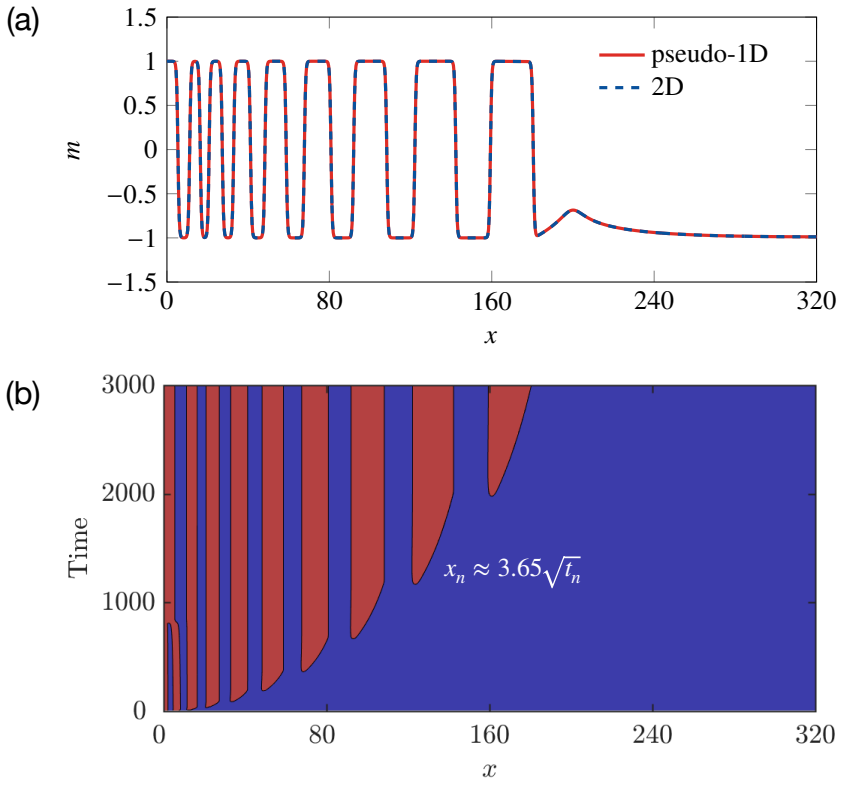


**Figure 3.** a) $m$ distributions comparison of the pseudo-1D and 2D simulations at time $t = 3000$ along $x$-axis and b) $m$ spatio-temporal evolution along $x$-axis.

terns. The numerical results are reproducing observations from controlled laboratory experiments supporting the argument that an approach based on material balances and first principles is a promising strategy for analysis of the empirical laws (Droz et al., 1999). The discrepancy of the model result at the top boundary is similar to the observations in laboratory experiments (Droz et al., 1999) where at the boundary condition Ostwald ripening effects (Ostwald, 1902) have been argued to overcome the clear definition of thin stripes in the wake of the propagating thicker leading bands (Ammar & Al-Ghoul, 2020).

The results from the pseudo-1D case are in perfect agreement with the extruded 2D case, as shown in Figure 2b and 3a. Therefore, for the sake of computational efficiency, we employ the pseudo-1D domain for parameter studies and Zebra rock sample calibration in Section 3.2 and 3.3. A real 2D scenario is considered for the transition from bands to spots in Section 3.4.

In what follows, we quantitatively verify our numerical results by investigating the behaviour of Liesegang striping in terms of the timing, spacing, Matalon-Packter law, and width laws. Figure 3a displays the thickness of the periodic stripes and interband spacing along the $x$-axis. First, the *timing law* indicates that the diffusion front advances proportionally to the square root of the time $x \propto \sqrt{t}$ (Morse & Pierce, 1903). Our results follow the linear relationship between the position of the $n$th band and the square root of its appearance time as $x_n \approx 3.65\sqrt{t_n}$, as Figure 3b shows. Next, the *spacing law* relates the location of subsequent stripes by $x_{n+1}/x_n = 1 + p$ where $1 + p$ is the spacing coefficient. The spacing coefficient $1+p > 0$ denotes the normal Liesegang stripes, whereas $1+p < 0$ represents the revert Liesegang stripes (Chopard et al., 1994; Karam et al., 2011). In this case, the estimated $1+p$ is around 1.25, denoting the normal Liesegang

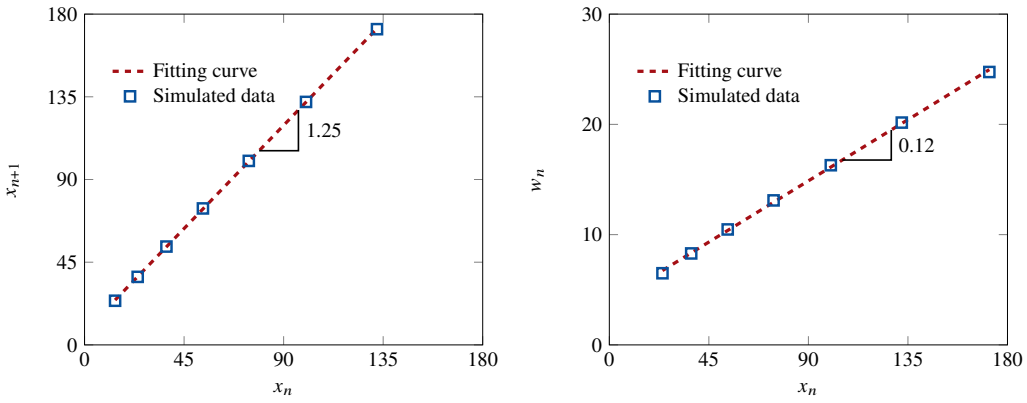


(a) Spacing law (b) Width law

**Figure 4.** a) Spacing and b) width laws verification of Liesegang band.

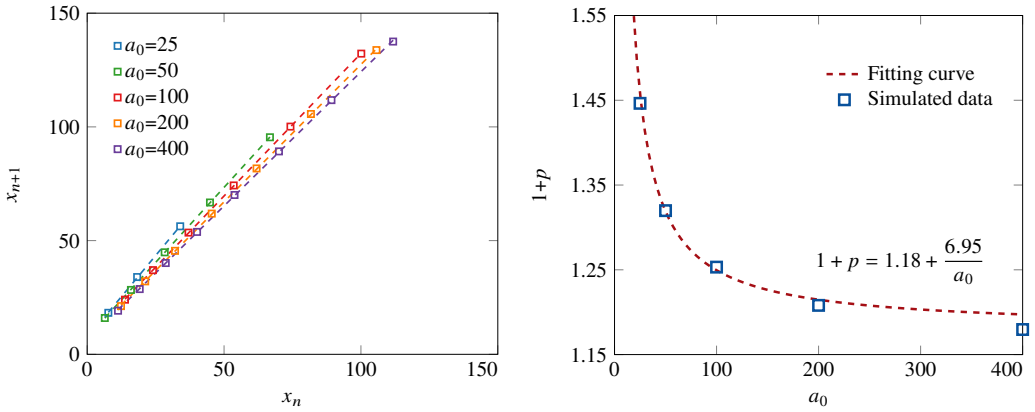


(a) Spacing laws for different $a_0$ (b) Spacing coefficients versus $a_0$

**Figure 5.** Verification of Matalon-Packter law for Liesegang stripes: a) spacing laws for different $a_0$ and b) spacing coefficient versus $a_0$.

stripes as Figure 4a shows. Additionally, the phenomenological *Matalon-Packter law*

$$p = F(b_0) + G(b_0)\frac{b_0}{a_0}$$

associates the parameter $p$ with the initial concentrations of the reagents $A$ and $B$ (Matalon & Packter, 1955). We increase the outer reagent $a_0$ from 25 to 400 and fit the spacing coefficient by an inverse function as $1+p = 1.18+6.95/a_0$ in Figure 5, demonstrating that our numerical method reproduces the spacing and Matalon-Packter laws. Finally, the *width law* states that the band width $w_n$ is proportional to the position $x_n$ of the band as $x_n \propto w_n$. The linear relationship between $x_n$ and $w_n$ is demonstrated in Figure 4b. With all the four empirical laws observed in the Liesegang phenomenon being successfully reproduced, the model is properly benchmarked. Interestingly we obtain similar evolution patterns with coarser resolution in space and time when we simulate in true 2D simulation of the strip. We, however, still proceed with the higher accuracy provided by the pseudo-1D simulation for the parameter studies as presented in Section 3.2 and the numerical inversion of Zebra rock patterns in Sections 3.3 and 3.4.

### 3.2 Diffusive coefficients

Three diffusive coefficients appear in the governing equation (8): the self-diffusion coefficients $D_a$ and $D_b$ of the reagents $A$ and $B$ and diffusive mobility $\lambda$ of the product $C$ emerging from the Cahn-Hilliard dynamics. The self-diffusion coefficient ratio $\theta = D_a/D_b$ parametrizes the influence of the self-diffusion coefficients. We assume that $D_a > D_b$ according to (Dayeh et al., 2014; Al-Ghoul et al., 2009) (i.e., the diffusivity of $Fe^{2+}$ is smaller than the counterpart of $O^{2-}$). Thus, we vary $D_a$ and $\lambda$ but fix $D_b = 1$ in our studies. Figure 6 displays the spacing laws in terms of $\theta$=1, 2, 3, 4, 5, 7, 9 and 10. Parameters $\theta$ and $1+p$ are correlated by plotting the ratio of the self-diffusion coefficient versus the spacing coefficient, as shown in Figure 6b.

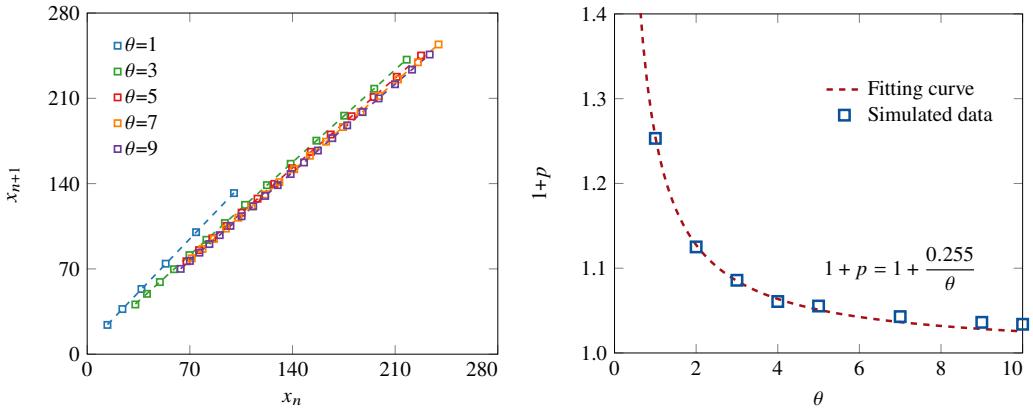


(a) Spacing law for different $\theta$

(b) Spacing coefficient versus $\theta$

**Figure 6.** Spacing laws for different self-diffusion coefficient ratios $\theta$=1, 2, 3, 4, 5, 7, 9, 10: a) spacing laws for different $\theta$ and b) spacing coefficients versus $\theta$.

Our results confirm that the spacing coefficient is in a hyperbolic relationship with the ratio of self-diffusion coefficients, as reported by Itatani et al. (2021). A high diffusivity ratio $\theta$ effectively decreases the distance between adjacent stripes, as the phenomenological Matalon-Packter law predicts. Increasing the diffusion coefficient $D_a$ is similar to raising the concentration of the outer reagent $A$ decreasing $p$ and the relative thickness of the stripes. Using the phenomenological Matalon-Packter law, we fit the nonlinear numerical results using a hyperbola

$$1 + p = 1 + \frac{0.255}{\theta}$$

This allows us to determine the self-diffusion coefficient ratio from field measurements of Zebra rock patterns.

We investigate the effect of Cahn-Hilliard diffusional dynamics on the spacing by sampling $\lambda$ between 0.1 and 0.9 with 0.2 increments. Figure 7 depicts the spacing coefficients $1+p$ for different $\lambda$ values. Contrary to the self-diffusivities, a high Cahn-Hilliard diffusive mobility of the product $\lambda$ increases the spacing coefficient, where the increment is linear as Figure 7b shows

$$1 + p = 1.01 + 0.25\lambda$$

This linear relationship will prove useful in geological and industrial applications. Once we measure the spacing coefficient of a given sample, we can calibrate $\lambda$ to match the existing Liesegang patterns. Given the key factors affecting $\lambda$ in experiments and geological applications, we optimize the process to achieve the expected Liesegang patterns.

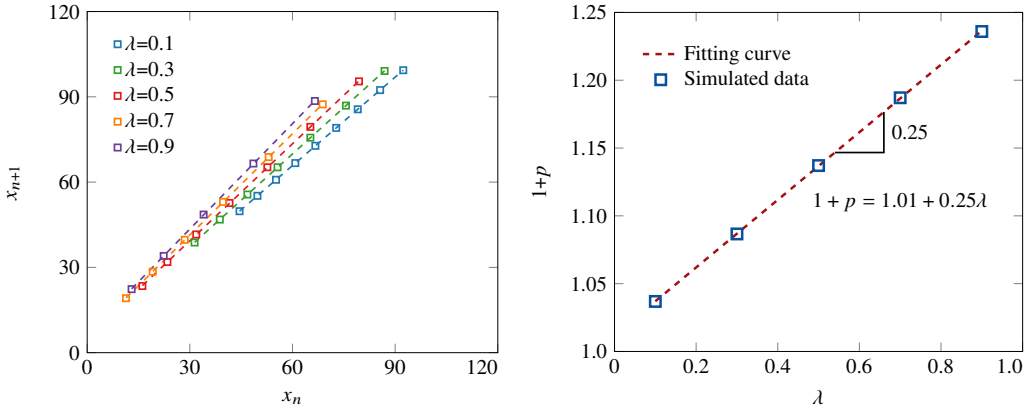


(a) Spacing laws for different $\lambda$ (b) Spacing coefficients versus $\lambda$

**Figure 7.** Spacing laws for different Cahn-Hilliard diffusive mobilities $\lambda$=0.1, 0.3, 0.5, 0.7, 0.9: a) spacing laws for different $\lambda$ and b) spacing coefficients versus $\lambda$.

### 3.3 2D Liesegang stripes in Zebra rocks

In this section we analyze the regular patterns appearing in Zebra rocks quantitatively. The distinct Zebra patterns are associated with the interaction between the diffusion and reaction processes. In this study, we assume the reaction rate constant and vary the diffusive coefficients by modifying either the self-diffusion coefficients or the Cahn-Hilliard diffusive mobility. For a given Zebra rock sample, we first measure the spacing coefficient $1+p$ as Table 2 lists. The measured $1+p$ enables us to estimate the corresponding combinations of the self-diffusion ratio $\theta$ and the Cahn-Hilliard diffusive mobility $\lambda$. Finally, we rely on our numerical model with varying combination of coefficients to fit with the Zebra patterns. We report four examples of Zebra rock samples being successfully reproduced with optimized coefficients, as follows.

**Table 2.** Measured spacing coefficients and estimated self-diffusion coefficients and Cahn-Hilliard diffusive mobilities for four Zebra rock samples.

| Sample number | 1 | 2 | 3 | 4 |
|---|---|---|---|---|
| Measured spacing coefficients $1+p$ | 1.071 | 1.060 | 1.054 | 1.000 |
| Estimated ratios of self-diffusion coefficients $\theta$ | 1.0 | 4.25 | 4.72 | 7.0 |
| Estimated Cahn-Hilliard diffusive mobilities $\lambda$ | 0.244 | 1.0 | 1.0 | 0.1 |

For the Zebra rock sample 1 in Figure 8 from Mattievich et al. (2003), we find that the formed patterns follow both the spacing and width laws as shown in Figure 9. We scale the band position $x_n$ and its width $w_n$ by a chosen cross-section whose length is represented by the green axis and fit the measured data as a linear line. The slope corresponding to the spacing coefficient is estimated to be around 1.071. Also, $1+p = 1.071$ corresponds to a $\lambda$ in the range of 0.1 to 0.3 based on Figure 7b when fixing the ratio of self-diffusion coefficient $\theta = 1.0$. After choosing the combination $\theta = 1.0$ and $\lambda = 0.244$ based on the linear relationship $1+p = 1.01+0.25\lambda$, the numerical results show a good agreement with the Zebra rock sample with reference to the formed patterns, as demonstrated in Figure 8. This similarity is also found in Figure 9a where the simulated band locations match with the measured band locations. The fitting curve based on the

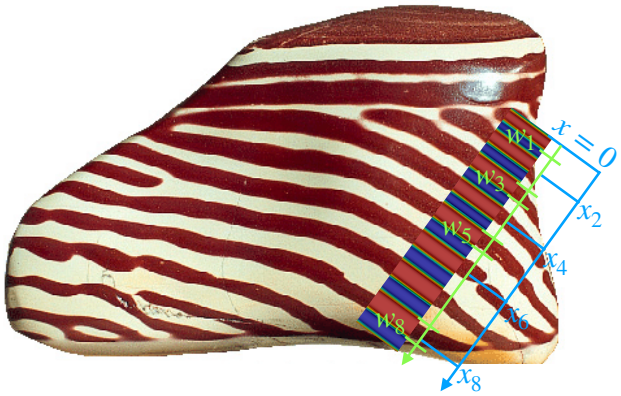


**Figure 8.** Pattern comparison between the simulated results and the Zebra rock sample 1 modified from Mattievich et al. (2003).

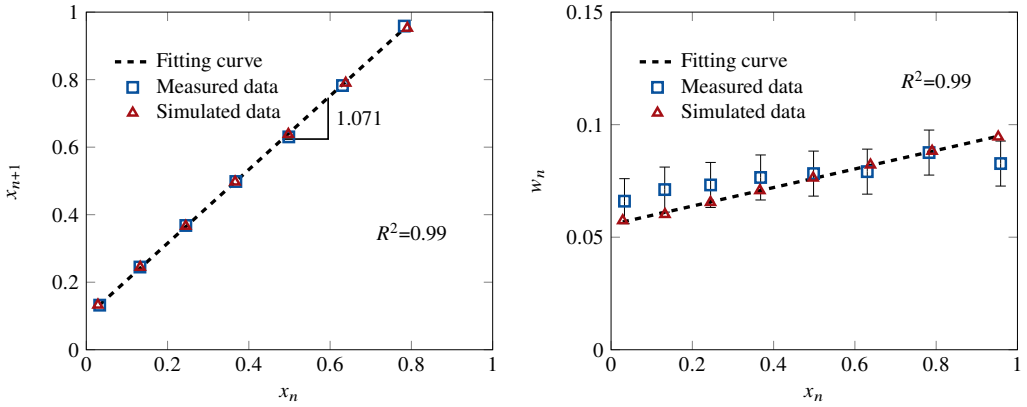


(a) Measured and simulated spacing laws

(b) Measured and simulated width laws

**Figure 9.** Comparison between the Zebra rock sample 1 and its numerical results for a) spacing and b) width laws.

simulated data yields a high R-square value $R^2 = 0.99$, indicating a strong linear relationship of the spacing law reproduced using our numerical workflow. In addition, we compare the thickness of the measured stripes and the simulated stripes. Given the variation in the measured thickness of the natural stripe patterns, we plot the scaled measured widths with standard deviations. Figure 9b shows that the difference between the simulated and measured width is within an acceptable range.

In what follows we use two Zebra rock samples from the Western Australian Museum (see Figure 10a and 12a) to quantitatively investigate the effect of the self-diffusion coefficients. As the diffusion fronts are not one-dimensional in both samples, indicated by the curved stripes, we draw a curved green axis along the normal direction of each band to approximate the principal diffusion direction. Figure 10b and 12b represent the Liesegang stripes along the curved cross-sections allowing to estimate the spacing coefficients. The measured spacing coefficients $1 + p$ are 1.060 and 1.054, respectively, for the Zebra rock samples 2 and 3. Thus, according to Figure 6b, we choose the ratio of self-diffusion coefficients $\theta = 4.25$ and 4.72 while fixing the Cahn-Hilliard diffusive mobility $\lambda = 1.0$. Figures 11 and 13 show that the simulated spacing and width laws are nearly identical to those from Zebra rock sample measurements when using the estimated parameters.

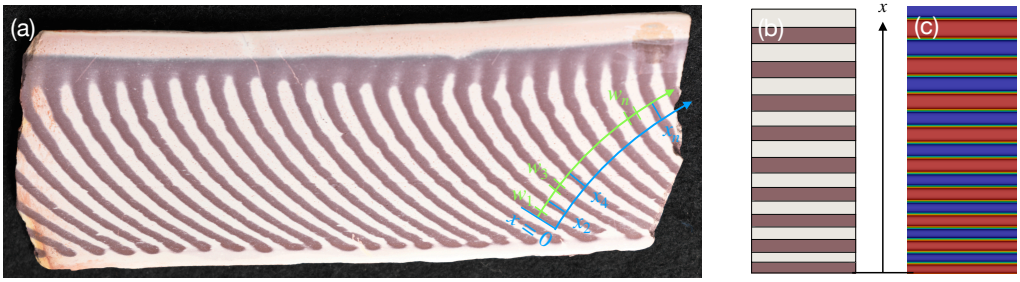


**Figure 10.** a) Zebra rock sample 2, b) measured stripes along the curved diffusion direction, and c) simulated bands.

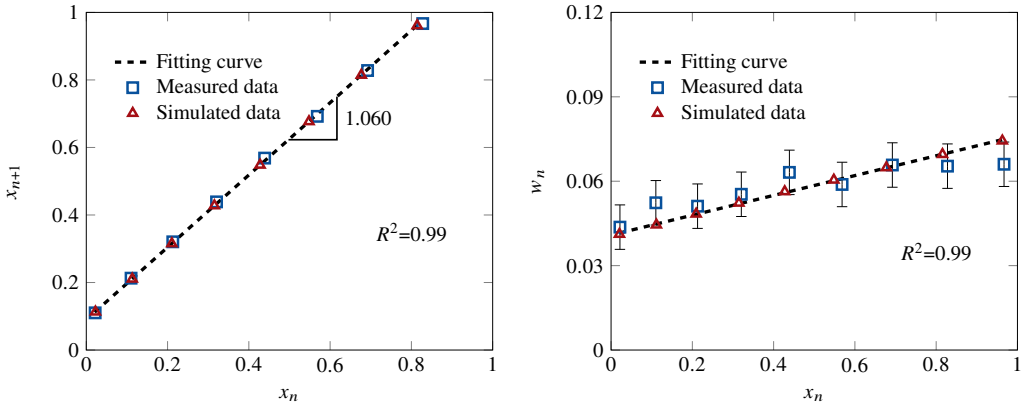


(a) Measured and simulated spacing laws

(b) Measured and simulated width laws

**Figure 11.** Comparison between the Zebra rock sample 2 and its numerical results for a) spacing and b) width laws.

As a special end-member uniform constant width and spacing patterns are observed in Zebra rocks, as Figure 14 exemplifies. This may indicate the tendency for the Zebra rock patterns to form under very slow dynamic processes close to the ideal stationary Turing pattern (slope zero on the width law in Figure 14b). The uniform pattern also implies negligible variations between stripes, indicating the spacing coefficient is $1+p \approx 1$, following the classical Turing pattern (see steady wave solutions in Hu et al. (2022)). As Figures 6b and 7b suggest, a combination of the large ratio of the self-diffusion coefficient $\theta$ and the small Cahn-Hilliard diffusive mobility $\lambda$ generates a small spacing coefficient. Here, setting $\theta = 7.0$ and $\lambda = 0.1$ can reproduce the regular pattern and the quantitatively matches the data as Figure 15 presents. We therefore conclude that our working hypothesis that Liesegang pattern can be directly used for derivation of key physical parameters using e.g., simple computer-vision analysis, is proven.

### 3.4 Transition from stripes to spots in Zebra rocks

In addition to the regular and uniform Liesegang stripes arising in Zebra rocks, there are two other categories of irregular patterns; these are patterns with intermixed stripes and spots and pure spot patterns as Figure 16a-b and Figure 16c show, respectively. The transition between stripes and spots in Zebra rocks is barely addressed in the literature. In this section we present a first-step numerical investigation underlying the role that the diffusive mobility $\lambda$ plays in generating diverse patterns. Figure 16a-c illustrate the three stages of the transition: (i) stripes separating into connected spots, as shown in

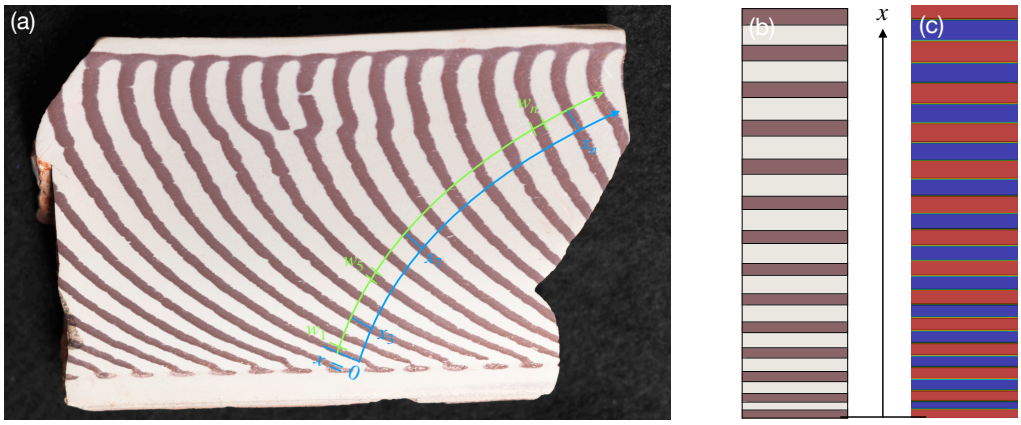


**Figure 12.** a) Zebra rock sample 3, b) measured stripes along the curved diffusion direction, and c) simulated bands.

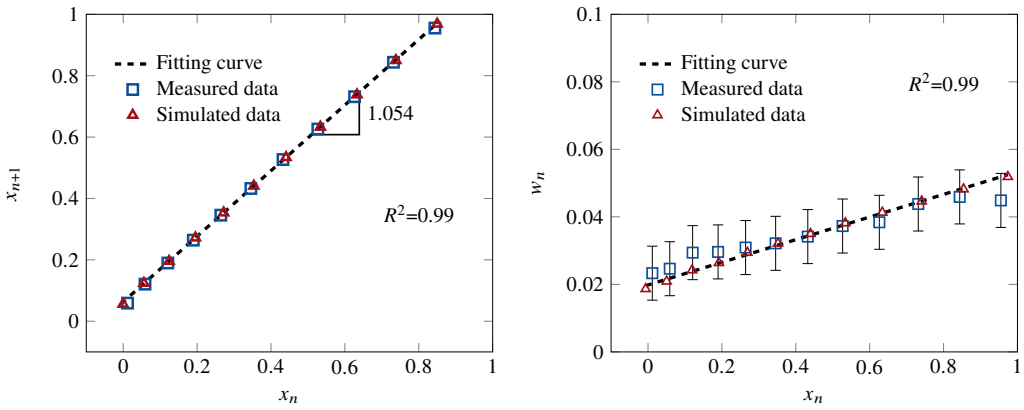


(a) Measured and simulated spacing laws

(b) Measured and simulated width laws

**Figure 13.** Comparison between the Zebra rock sample 3 and its numerical results for a) spacing and b) width laws.

Figure 16a, (ii) a following development into partly connected spots, as observed in Figure 16b, and (iii) full development into isolated spots, as shown in Figure 16c.

Based on the phase separation model, three parameters control the transition from stripes to spots in a reaction-diffusion system (Wang et al., 2015; Dayeh et al., 2014; Al-Ghoul et al., 2009), namely, the Cahn-Hilliard diffusive mobility $\lambda$, the noise distribution $\eta_c$, and the initial reagent concentration distribution. A random noise $\eta_c$ with a uniform distribution in $[-0.01, 0.01]$ is applied to the equation (8) as the imposed system inhomogeneity. We vary $\lambda$ and the initial distribution of reagents to capture Liesegang striping in irregular Zebra patterns, containing both spots and stripes.

To reduce the computational cost, the system size is set to half of the 2D scenario, $L_x = 160$ and $L_y = 32$ with a uniform grid $1280\times256$ in the $x$- and $y$-directions, respectively, and the time step increases two times to $\Delta t = 5\times10^{-5}$. Modified parameters compared to those given in Section 3.1 include $\gamma = 0.15$, the initial condition $b_0 = 0.5$ and $m_0 = -1.5$. Figure 17 displays the simulation results of the product distribution patterns for $\lambda$ varying from 0.1 to 0.6 with a 0.1 increment at the same time $t = 200$, respectively. A combination of spotted and striped patterns is shown in all patterns with a trend that a smaller $\lambda$ leads to smaller size (and hence denser distribution of) spots.

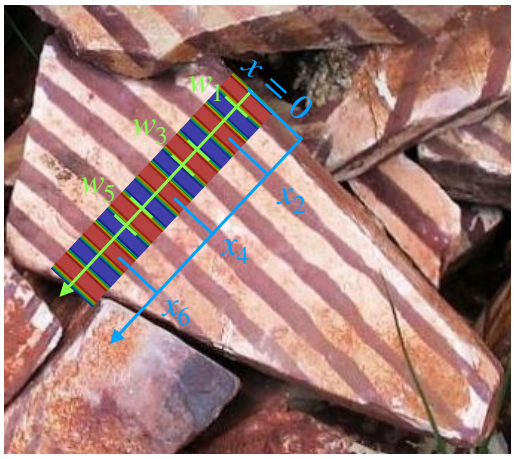


**Figure 14.** Pattern comparison between the Zebra rock sample 4 and its numerical results.

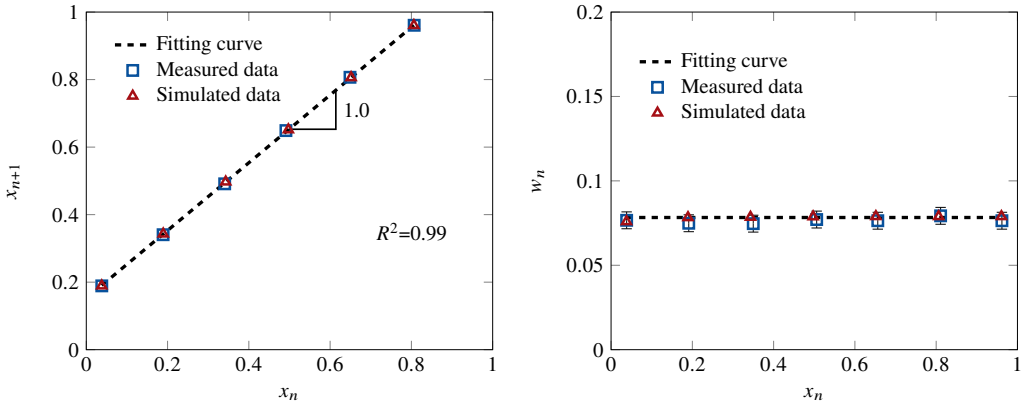


(a) Measured and simulated spacing laws

(b) Measured and simulated width laws

**Figure 15.** Comparison between the Zebra rock sample 4 and its numerical results for a) spacing and b) width laws.

For example, the $\lambda = 0.1$ case resembles the fully developed spotted pattern in Figure 16c. For larger values of $\lambda \geq 0.2$, the transition from stripes to spots is less complete as a higher diffusive mobility of the product essentially promotes Ostwald ripening.

Figure 18 further shows the time evolution of the pattern forming process for the case $\lambda = 0.2$ from $t = 100$ to $t = 250$, revealing the time-lapse transition from stripes to spots. It is observed that as time progresses part of the stripes gradually localize into spots as a result of the imposed heterogeneity. Later on (from $t = 200$ to $t = 250$) we note an interesting feature that the evolution of these localized spots pattern is overtaken by the Ostwald ripening effect. Overall, we find the trend that for cases of $\lambda < 0.2$, the *stripes localizing into spots* phenomenon is prominent over the entire domain while for cases of $\lambda \geq 0.2$, such type of localization instability is regional, Ostwald ripening dominantes over localization at global scale.

## 4 Discussion and Conclusions

This paper describes the Liesegang striping process using a phase-field model that describes a plethora of Mississippi Valley Type mineralization patterns such as observed

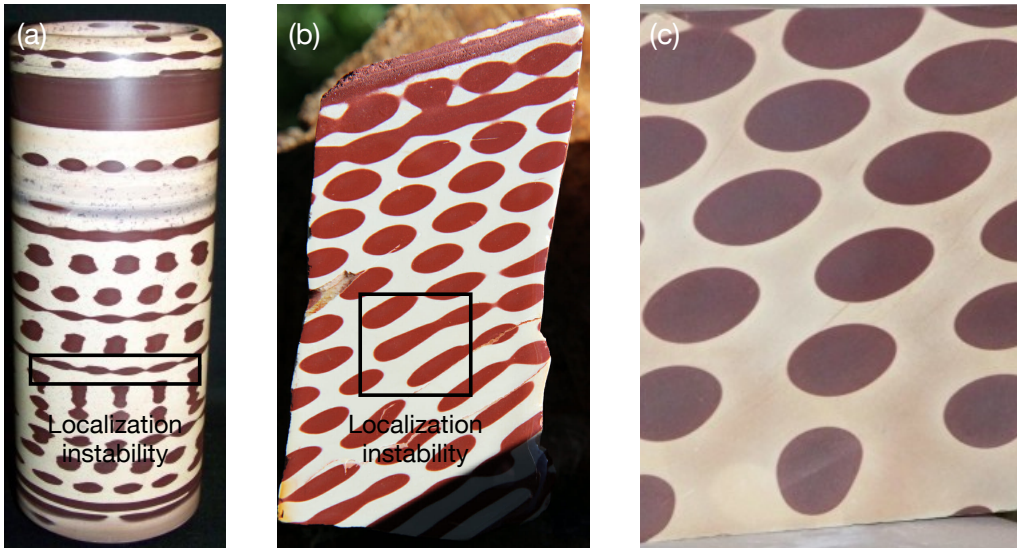


**Figure 16.** Stripe-to-spot transition in Zebra rocks: combined patterns with stripes and a) connected spots and b) partly connected spots , and c) isolated spot patterns.

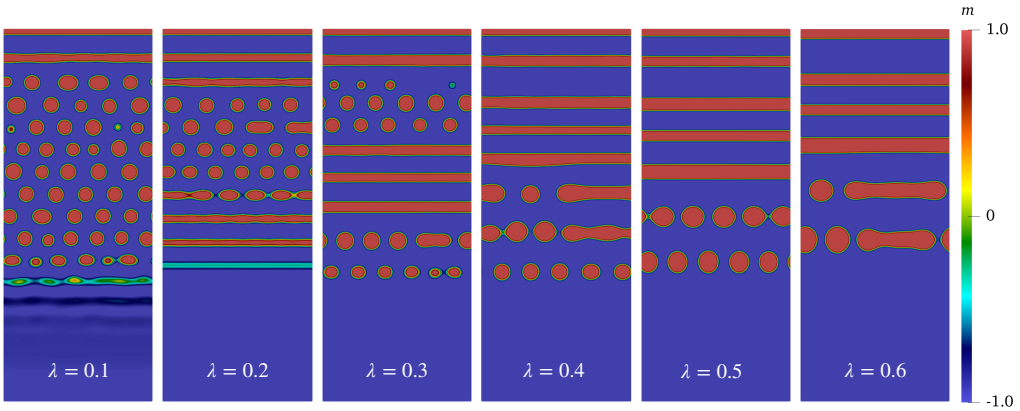


**Figure 17.** Stripe-to-spot transition for different Cahn-Hilliard diffusive mobilities ranging from 0.1 to 0.6 at $t = 200$ in the domain's upper half $L_x \in [0, 80]$. The scaled parameters used are $\bar{a} = 100$, $a_0 = 0$, $b_0 = 0.5$, $m_0 = -1.5$, $D_a = D_b = 1.0$, $\kappa = 1.0$, $\varepsilon = 1.0$, $\gamma = 0.15$, $\sigma = 0.2$, and $\eta_c \in [-0.01, 0.01]$.

in Zebra rocks. Quantitatively, we find that the diffusive coefficients, including self-diffusivity coefficients and Cahn-Hilliard diffusive mobility, significantly affect the pattern spacing and width, thereby offering a quantitative analysis tool for a given reaction-diffusion system; specifically for the case of regular Zebra rock patterns which can be modelled in pseudo-1D as a 2D system.

In earlier numerical studies, the dynamics of Ostwald ripening between the leading front and the trailing bands of the propagating dissolution-precipitation reaction front was proposed to lead to the observed scaling behavior and to the mass oscillation in the bands (Mansour & Al-Ghoul, 2015). This earlier numerical analysis also uses a reaction-diffusion formalism but employs an arbitrary Heaviside function to prevent total dissolution of the precipitation bands formed by the reaction product (here hematite). Our model refines this simplification and considers the reaction product mobility governing

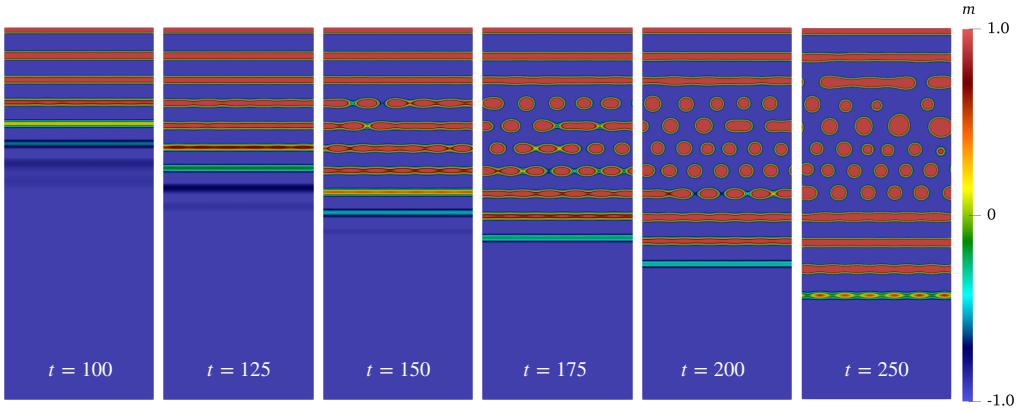


**Figure 18.** Localization instability triggers stripe-to-spot transition for $\lambda$=0.2 in the domain's upper half $L_x \in [0, 80]$.

the double well kinetics of the spinodal decomposition in the Cahn-Hilliard approach to prevent total dissolution of the bands. This inclusion of additional dynamics does not appear to change the qualitative findings of the numerical earlier studies but is important for quantitative inversion of the dynamic parameters. For low mobility values this can lead in particular to the phenomenon of a transition from bands to spots which is not captured by the Heaviside function approach. The inclusion of Cahn-Hilliard dynamics is therefore an important ingredient for a minimalist model of the pattern formation in Zebra rock.

To model this transition of pattern evolution towards more complex and irregular geometries true 2D simulations were required. Of particular interest is the dynamic evolution from striped patterns into spot patterns or combined stripes and spots. For the transition from stripes to spots the magnitude of the Cahn-Hilliard diffusive mobility of the product is identified as a key parameter. This interesting dynamic phenomenon deserves future follow-up studies for quantitative inversion. In this study we reproduce qualitatively a diverse set of spotted Zebra rock patterns by varying the Cahn-Hilliard diffusive mobility $\lambda$. For example, $\lambda < 0.2$ produces spotted patterns, while for $\lambda \geq 0.2$, the patterns transition into a combination of stripes and spotted patterns. We therefore conclude that the Cahn-Hilliard diffusive mobility may be used in future studies to predict the transition patterns when spots and stripes both exhibit. For the case of regular quasistatic Zebra bands the model allows us to accurately estimate diffusivities from photographic evidence.

Future work will consider the assimilation of additional data to explain various geochemical and hydromechanical phenomena and predict potential energy and mineral resources. The formation of these striped patterns requires special redox conditions which were particularly favourable during the Archean, where commercially attractive banded iron formations formed (Condie, 2016). These resemble strongly the Zebra band patterns investigated here. The banded iron formations are laminated chemical reactive sediments that have an iron content larger than 15-30%. They show as distinct events in the time series of the Archean where following the great Earth oxidation event oxygen content in the seawater fluctuated strongly from basically anoxic at depth to strongly oxidated following a glaciation event (Holland, 2006). A thorough investigation of their style with our model might be developed into an outcrop exploration tool conveniently based on aerial photographs or drone images. Moreover, if the method can be used with confidence to identify high-grade ores, the numerical workflow as presented here can help in quantifying and optimising resource recovery with energy and cost savings for recovery, trans-

port and crushing. The finding that the basic width, spacing and Matalon-Pakter laws can be reliably inverted from the observed images using relatively coarse meshes may open an entirely new scope of geophysical field exploration techniques.

**Acknowledgments**

The authors wish to first of all acknowledge the generous support of the Western Australian Museum for the supply of the high quality images of Zebra Rock in particular Geoff Deacon for taking the photos and the curator Peter Downes for managing the request. The support of the Research Grant Council of Hong Kong (ECS 27203720 and GRF 17206521) and the Australian Research Council (ARC DP170104550, DP170104557, DP200102517, LP170100233) is acknowledged. The funding from the European Union's Horizon 2020 research and innovation programme under the Marie Sklodowska-Curie grant agreement No 777778 (MATHROCKS) is acknowledged.

**Data Availability Statement:** The Finite Element Method code and simulation data can be downloaded from Mendeley Data via

https://data.mendeley.com/v1/datasets/sjjw5ctwfh/draft?a=5222ece1-4366-478c-a451-2c0641af2e29

## References

Abrajevitch, A., Pillans, B. J., Roberts, A. P., & Kodama, K. (2018). Magnetic Properties and Paleomagnetism of Zebra Rock, Western Australia: Chemical Remanence Acquisition in Hematite Pigment and Ediacaran Geomagnetic Field Behavior. *Geochemistry, Geophysics, Geosystems*, *19*(3), 732–748.

Al-Ghoul, M., Ghaddar, T., & Moukalled, T. (2009). Pulse-front propagation and interaction during the growth of CdS nanoparticles in a gel. *The Journal of Physical Chemistry B*, *113*(34), 11594–11603.

Al-Ghoul, M., & Sultan, R. (2019). Simulation of geochemical banding: Theoretical modeling and fractal structure in acidization-diffusion-precipitation dynamics. *Physical Review E*, *100*(5), 052214.

Ammar, M., & Al-Ghoul, M. (2020). Band Propagation, Scaling Laws, and Phase Transition in a Precipitate System III: Effect of the Anions of Precursors. *Journal of Physical Chemistry A*, *124*(1), 39–45.

Antal, T., Droz, M., Magnin, J., Pekalski, A., & Rácz, Z. (2001). Formation of Liesegang patterns: Simulations using a kinetic Ising model. *The Journal of Chemical Physics*, *114*(8), 3770–3775.

Antal, T., Droz, M., Magnin, J., & Rácz, Z. (1999). Formation of Liesegang patterns: A spinodal decomposition scenario. *Physical Review Letters*, *83*(15), 2880.

Antal, T., Droz, M., Magnin, J., Rácz, Z., & Zrinyi, M. (1998). Derivation of the Matalon-Packter law for Liesegang patterns. *The Journal of Chemical Physics*, *109*(21), 9479–9486.

Arguello, M. E., Gumulya, M., Derksen, J., Utikar, R., & Calo, V. M. (2022). Phase-field modeling of planar interface electrodeposition in lithium-metal batteries. *Journal of Energy Storage*, *50*, 104627.

Arguello, M. E., Labanda, N. A., Calo, V. M., Gumulya, M., Utikar, R., & Derksen, J. (2022). Dendrite formation in rechargeable lithium-metal batteries: Phase-field modeling using open-source finite element library. *Journal of Energy Storage*, *53*, 104892.

Arndt, D., Bangerth, W., Blais, B., Clevenger, T. C., Fehling, M., Grayver, A. V., ... Wells, D. (2020). The `deal.II` Library, Version 9.2. *Journal of Numerical Mathematics*, *28*(3), 131-146.

Badr, L., Moussa, Z., Hariri, A., & Sultan, R. (2011). Band, target, and onion pat-

terns in $Co(OH)_2$ Liesegang systems. *Physical Review E*, *83*(1), 016109.

Büki, A., Kárpáti-Smidróczki, É., & Zrínyi, M. (1995). Computer simulation of regular Liesegang structures. *The Journal of Chemical Physics*, *103*(23), 10387–10392.

Cahn, J. W. (1961). On spinodal decomposition. *Acta Metallurgica*, *9*(9), 795-801.

Cahn, J. W., & Hilliard, J. E. (1958). Free Energy of a Nonuniform System. I. Interfacial Free Energy. *The Journal of Chemical Physics*, *28*(2), 258-267.

Chopard, B., Luthi, P., & Droz, M. (1994). Reaction-diffusion cellular automata model for the formation of Leisegang patterns. *Physical Review Letters*, *72*(9), 1384.

Christoph, J., Strasser, P., Eiswirth, M., & Ertl, G. (1999). Remote triggering of waves in an electrochemical system. *Science*, *284*(5412), 291–293.

Condie, K. C. (2016). Chapter 8 - the atmosphere and hydrosphere. In *Earth as an evolving planetary system (third edition)* (p. 237-278). Academic Press.

Cooper, B. (2012). The incomputable reality. *Nature*, *482*(7386), 465–465.

Dayeh, M., Ammar, M., & Al-Ghoul, M. (2014). Transition from rings to spots in a precipitation reaction–diffusion system. *RSC advances*, *4*(104), 60034–60038.

DeWitt, S., Rudraraju, S., Montiel, D., Andrews, W. B., & Thornton, K. (2020). PRISMS-PF: A general framework for phase-field modeling with a matrix-free finite element method. *npj Computational Materials*, *6*(1), 1–12.

Droz, M., Magnin, J., & Zrinyi, M. (1999). Liesegang patterns: Studies on the width law. *The Journal of Chemical Physics*, *110*(19), 9618-9622.

Geidans, L. (1981). Zebra rock of Western Australia. In *Geological society of australia, abstracts* (Vol. 3, p. 22).

Hancock, P. (1968). Location and investigation of zebra rock occurrences, East Kimberley region. *Geological Survey of Western Australia, Annual Report*, 67–68.

Hantz, P., & Biró, I. (2006). Phase separation in the wake of moving fronts. *Physical Review Letters*, *96*(8), 088305.

Hedges, E. S., & Henley, R. V. (1928). The formation of liesegang rings as a periodic coagulation phenomenon. *Journal of the Chemical Society*, 2714–2727.

Hobson, R. A. (1930). Zebra rock from the East Kimberley. *Journal of the Royal Society of Western Australia*, *16*, 57–70.

Holba, V., & Fusek, F. (2000). Gravity Effect on the Formation of Periodic Precipitation Patterns. *Collection of Czechoslovak Chemical Communications*, *65*(9), 1438–1442.

Holland, H. D. (2006). The oxygenation of the atmosphere and oceans. *Philosophical Transactions of the Royal Society B: Biological Sciences*, *361*(1470), 903–915.

Hu, M., Sun, Q., Schrank, C., & Regenauer-Lieb, K. (2022). Cross-scale dynamic interactions in compacting porous media as a trigger to pattern formation. *Geophysical Journal International*, *230*(2), 1280-1291.

Itatani, M., Fang, Q., & Nabika, H. (2021). Modification of the Matalon–Packter Law for Self-Organized Periodic Precipitation Patterns by Incorporating Time-Dependent Diffusion Flux. *The Journal of Physical Chemistry B*, *125*(25), 6921–6929.

Karam, T., El-Rassy, H., & Sultan, R. (2011). Mechanism of Revert Spacing in a $PbCrO_4$ Liesegang System. *The Journal of Physical Chemistry A*, *115*(14), 2994–2998.

Kawahara, H., Yoshida, H., Yamamoto, K., Katsuta, N., Nishimoto, S., Umemura, A., & Kuma, R. (2022). Hydrothermal formation of Fe-oxide bands in zebra rocks from northern Western Australia. *Chemical Geology*, *590*, 120699.

Kelka, U., Veveakis, M., Koehn, D., & Beaudoin, N. (2017). Zebra rocks: compaction waves create ore deposits. *Scientific Reports*, *7*(1), 1–9.

Larcombe, C. (1924). Rock specimens from Ord River and Oakover River respectively. *Geological Survey of Western Australia, Annual Report*, *19*.

Larcombe, C. (1926). Some rocks from four miles east of Argyle Station, Ord River, King district, Kimberley division. *Geological Survey of Western Australia, Annual Report*, *23*.

Liesegang, R. E. (1906). Eine scheinbar chemische Fernwirkung. *Annalen der Physik*, *324*(2), 395-406.

Loughnan, F., & Roberts, F. (1990). Composition and origin of the 'zebra rock' from the East Kimberley region of Western Australia. *Australian Journal of Earth Sciences*, *37*(2), 201–205.

Mansour, A. A., & Al-Ghoul, M. (2015). Band Propagation, Scaling Laws, and Phase Transition in a Precipitate System. 2. Computational Study. *The Journal of Physical Chemistry A*, *119*(35), 9201–9209.

Matalon, R., & Packter, A. (1955). The Liesegang phenomenon. I. Sol protection and diffusion. *Journal of Colloid Science*, *10*(1), 46–62.

Mattievich, E., Chadwick, J., Cashion, J. D., Boas, J. F., Clark, M., & Mackie, R. (2003). Macroscopic ferronematic liquid crystals determine the structure of Kimberley Zebra Rock. In *27th ann. cond. matt. phys. meet. conf. handb.*

May, S. M., Hoffmeister, D., Wolf, D., & Bubenzer, O. (2019). Zebra stripes in the Atacama Desert revisited–Granular fingering as a mechanism for zebra stripe formation? *Geomorphology*, *344*, 46–59.

Morsali, M., Khan, M. T. A., Ashirov, R., Holló, G., Baytekin, H. T., Lagzi, I., & Baytekin, B. (2020). Mechanical Control of Periodic Precipitation in Stretchable Gels to Retrieve Information on Elastic Deformation and for the Complex Patterning of Matter. *Advanced Materials*, *32*(10), 1905779.

Morse, H. W., & Pierce, G. W. (1903). Diffusion and supersaturation in gelatine. *Physical Review*, *17*(3), 129.

Msharrafieh, M., Al-Ghoul, M., Zaknoun, F., El-Rassy, H., El-Joubeily, S., & Sultan, R. (2016). Simulation of geochemical banding I: acidization-precipitation experiments in a ferruginous limestone rock. *Chemical Geology*, *440*, 42–49.

Müller, S. C., Kai, S., & Ross, J. (1982). Periodic precipitation patterns in the presence of concentration gradients. 1. Dependence on ion product and concentration difference. *The Journal of Physical Chemistry*, *86*(20), 4078–4087.

Nakouzi, E., & Steinbock, O. (2016). Self-organization in precipitation reactions far from the equilibrium. *Science Advances*, *2*(8), e1601144.

Nakouzi, E., & Sultan, R. (2011). Fractal structures in two-metal electrodeposition systems I: Pb and Zn. *Chaos: An Interdisciplinary Journal of Nonlinear Science*, *21*(4), 043133.

Ostwald, W. (1902). *Lehrbuch der allgemeinen Chemie* (Vol. 2). W. Engelmann.

Regenauer-Lieb, K., Hu, M., Schrank, C., Chen, X., Clavijo, S. P., Kelka, U., ... Jacquey, A. B. (2021). Cross-diffusion waves resulting from multiscale, multiphysics instabilities: theory. *Solid Earth*, *12*(4), 869–883.

Thomas, S., Lagzi, I., Molnár Jr, F., & Rácz, Z. (2013). Probability of the Emergence of Helical Precipitation Patterns in the Wake of Reaction-Diffusion Fronts. *Physical Review Letters*, *110*(7), 078303.

Wang, Y., Chan, M. A., & Merino, E. (2015). Self-organized iron-oxide cementation geometry as an indicator of paleo-flows. *Scientific Reports*, *5*(1), 1–15.